Surfaces and Interfaces 49 (2024) 104379

Contents lists available at ScienceDirect

Surfaces and Interfaces

journal homepage: www.sciencedirect.com/journal/surfaces-and-interfaces

Precise surface machining of fused silica using high stability atmospheric pressure microwave plasma jet with a new internal electrode

Chuansheng Wang [a], Bing Wu [a], Wei Hang [b,c,*], Dong Lu [a,*], Hui Deng [a,d,*]

[a] Department of Mechanical and Energy Engineering, Southern University of Science and Technology, Shenzhen, Guangdong, 518055, China
[b] College of Mechanical Engineering, Zhejiang University of Technology, Hangzhou, 310014, China
[c] Key Laboratory of Special Purpose Equipment and Advanced Processing Technology, Ministry of Education and Zhejiang Province, Zhejiang University of Technology, Hangzhou, 310014, China
[d] Shenzhen Engineering Research Center for Semiconductor-specific Equipment, Department of Mechanical and Energy Engineering, Southern University of Science and Technology, Shenzhen, Guangdong, 518055, China

ARTICLE INFO

Keywords:
Microwave plasma jet
Spline curve electrode
Plasma machining
Dwell time algorithm

ABSTRACT

Plasma is a promising approach for machining of fused glass substrates. Developing high-performance microwave torch is the core element to ensure the processing accuracy of this technology. In this study, a spline curve-based microwave torch internal electrode structure was proposed, which increased the internal electric field strength by 54 %. The discharge dynamics simulation based on this electrode shows that the plasma is excited at the inner electrode tip and the bottom of the resonant cavity, then it expands to form a linear discharge region and eventually fill the discharge tube. It was revealed by CCD images that with the increase of carrier gas flow rate, turbulent flow state appears in the tail of the jet. OES data shows that microwave Ar plasma can effectively dissociate CF_4, and due to the oxidation effect of oxygen, CF_x and C_2 content decrease significantly with the addition of oxygen. The machining experiment on fused silica shows that the material removal stability of this torch reaches 3.69 %, and the removal rate increases nY

arly with dwell time due to thermal effect. Finally, the machining performance of the atmospheric pressure microwave plasma jet was verified by figuring of a planar fused silica surface reducing the form error from 108.1 nm RMS to 16.5 nm RMS.

1. Introduction

Microwave plasma exhibits the superior characteristics such as high radical density and high processing efficiency. Consequently, it has been applied in various domains, including optical modification [1–4], elemental analysis [5,6], and surface treatment [7,8]. Among these applications, portable atmospheric pressure microwave plasma jet (AMPJ) represents a cutting-edge area of research in the field of microwave plasma technology owing to its simplified and versatile structure and the unnecessity of a vacuum system.

An AMPJ system generally consists of the following components: a microwave source, resonator cavity, short-circuit piston, nozzle (inner electrode), and other accessories [9]. The resonant cavity plays a crucial role in achieving an efficient microwave energy utilization. Microwaves enter the resonant cavity through a waveguide or coaxial line, and by adjusting the short-circuit piston, form a standing wave structure that enables the initial concentration of the electric field [10]. Both theoretical and experimental studies have demonstrated that the optimal distance from the short-circuit surface to the nozzle end is approximately $3\lambda/4$ [11]. The nozzle structure and the distance from the nozzle to the resonant cavity outlet are of great significance as they are key factors in achieving secondary electric field concentration for effective plasma excitation. It was reported that adjusting the T-shaped nozzle to a wedge-shaped nozzle enhances the electric field concentration ability, which aids in achieving efficient electric field breakdown. However, when using wedge nozzles, energy is distributed along the wedge surface, resulting in wide energy distribution space and limited energy utilization efficiency. Simulation results demonstrate that although placing the nozzle tip closer to the jet outlet improves discharge performance, the best discharge effect is achieved when the nozzle is positioned inside the jet outlet [12]. In practical experiments, when the nozzle too close to the jet outlet often leads to significant arc discharge

* Corresponding authors.
E-mail addresses: whang@zjut.edu.cn (W. Hang), lud@sustech.edu.cn (D. Lu), dengh@sustech.edu.cn (H. Deng).

https://doi.org/10.1016/j.surfin.2024.104379
Received 26 February 2024; Received in revised form 10 April 2024; Accepted 18 April 2024
Available online 22 April 2024

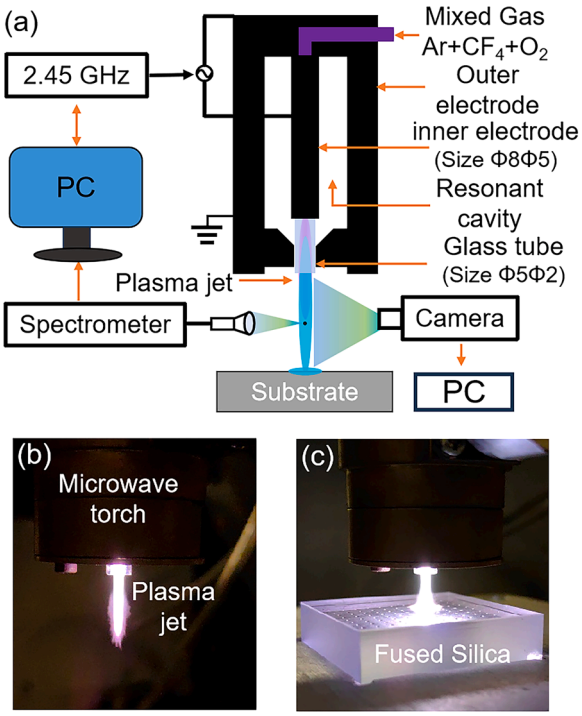

Fig. 1. (a) Schematic diagram of the AMPJ machining system, (b) Photo of the microwave plasma jet, (c) Photo of plasma jet machining of fused silica.

characteristics, which will damage and limit the life of the torch [13,14]. Therefore, it is very meaningful to optimize the inner electrode structure for improving the performance of microwave torch.

The surface form error of optics elements will cause the problems of phase difference and aberration [15]. Using non-destructive and ultra-precision machining technologies to enhance the surface form accuracy of optical components is an important solution for improving the imaging quality of optical systems. Plasma processing technology, known for its high efficiency and damage free characteristics, has been extensively researched over the past decade. This includes Capacitively Coupled Plasma (CCP) processing [16], Inductively Coupled Plasma (ICP) processing [17], and microwave processing technologies [7,10,18,19]. Compared to Capacitively Coupled Plasma (CCP) discharge plasma processing, microwave plasma jet material removal can achieve sub-millimeter full width half-maximum (FWHM), with a significantly broader bandwidth for machining surface form than CCP technology. Moreover, it possesses extremely high material removal stability, enabling it to also feature high-precision machining capabilities. Compared to Inductively Coupled Plasma (ICP) technology, microwave plasma jets operate at lower temperatures, which can eliminate local thermal stress caused by the high temperatures of ICP plasma and prevent material fragmentation issues due to thermal problems when machining crystalline materials. In summary, microwave plasma processing technology not only possesses the advantages of non-destructive and high-precision machining found in both CCP and ICP technologies but also offers broader bandwidth for surface form machining and a wider range of applicable materials. This technology has already been applied to various materials, such as fused silica, silicon, silicon carbide, and ULE [4,20-25].

The shape of the removed function and volume removal rate stability are crucial parameters that impact the accuracy of machining. These parameters are influenced by the jet topography and the gas recipe [26–28]. One of the studies on micro-plasma jet showed that when Ar was used as carrier gas, the O_2 quenching effect was severe, while He plasma was not quenched by O_2 [33,34], therefore, the plasma jet length of Ar carrier gas is shorter than that of He carrier gas. In addition to the

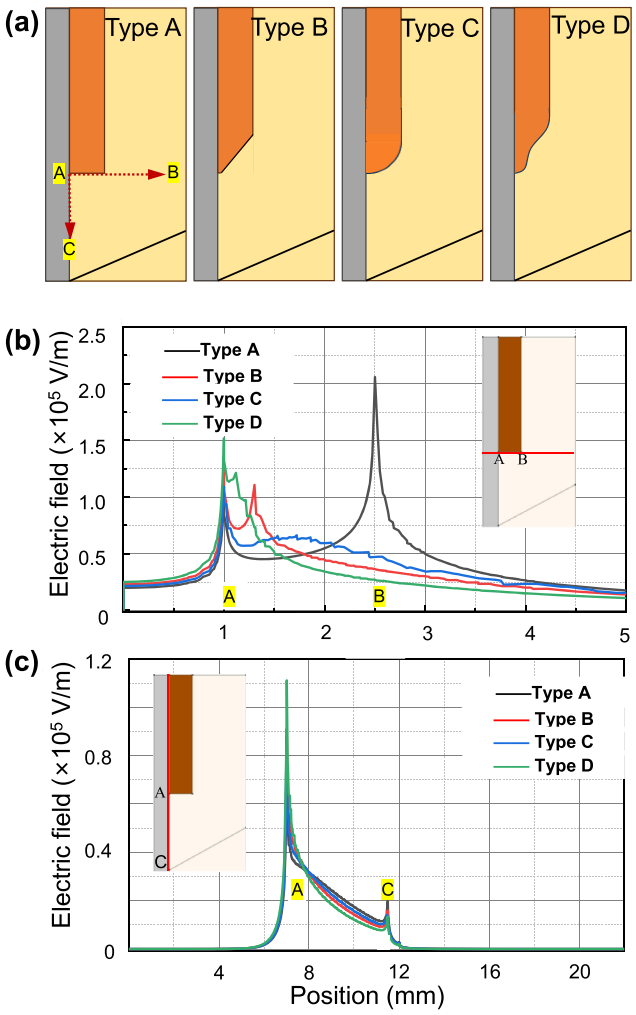

Fig. 2. (a) Four typical inner electrode structures, (b) The radial distribution of electric field, (c) The axial distribution of electric field.

Table 1
Electrical field intensity of point A in Fig. 2b.

Electrode type	A point electrical field intensity(V/m)
Initial	1.01×10^5
Electrode 1	1.12×10^5
Electrode 2	1.24×10^5
Electrode 3	1.55×10^5

Table 2
The main chemical reactions included in the simulation model.

Number	Reaction	Type of reaction	Energy(eV)
1	e+Ar→e+Ar	Elastic collision	0
2	e+Ar→e+Ar_m	Ground state excitation	11.5
3	e+Ar_m→e+Ar	Superelastic collision	−11.5
4	e+Ar→e+e+Ar+	Ground state ionization	15.8
5	e+Ar_m→e+e+Ar+	Cascade ionization	4.24
6	Ar_m+Ar_m→e+Ar+Ar^+	Penning ionization	–
7	Ar_m+Ar→Ar+Ar	Metastable quenching	–
8	Ar_m→Ar	Surface reaction	Adhesion coefficient 1
9	Ar→Ar	Surface reaction	Adhesion coefficient 1

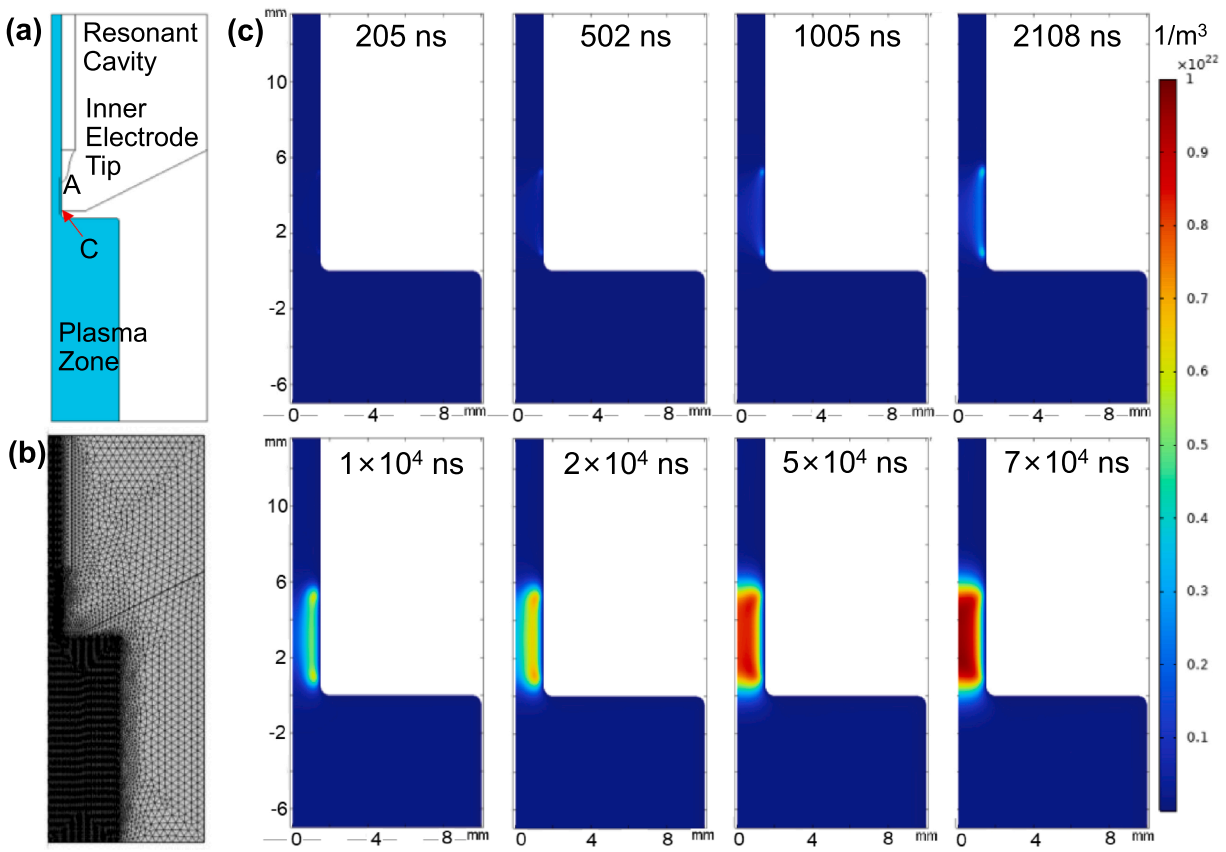

Fig. 3. (a) Simulation model, (b) Gridding of the model, (c) Evolution of plasma density distribution over time in microwave torch discharge.

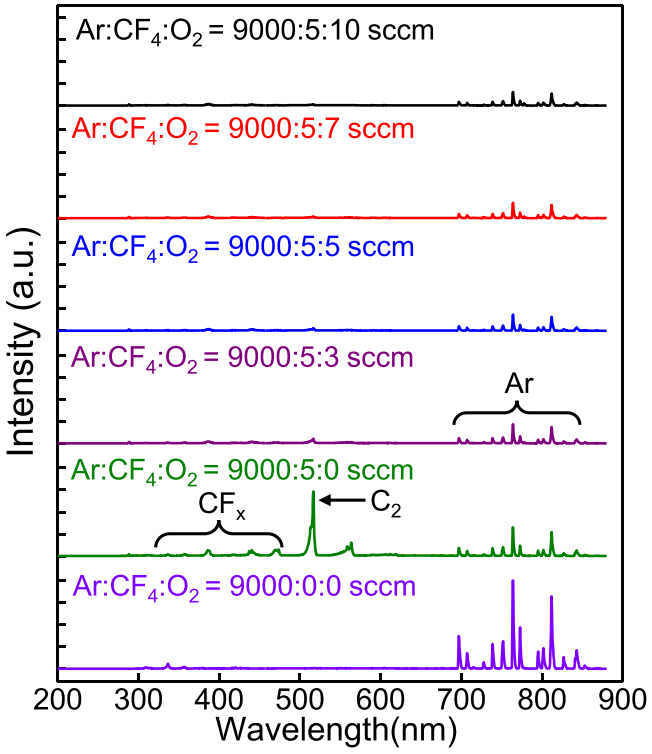

Fig. 4. Optical emission spectrum of the atmosphere microwave plasma jet.

type of carrier gas, the jet length increases as gas flow rate increases, it has been observed that the morphology of microwave jets exhibits a pattern of unsaturation-balance-supersaturation [35]. On the other hand, the addition of CF_4 leaded to the generation of various molecular radicals, which induced vibration and rotational excitation and facilitate energy transfer between different substances [29–32]. The relaxation time of this process exhibits significant variation, resulting in poor plasma stability and changes in jet length, in addition to the type of carrier gas, process components are key factors affecting the morphology of plasma jet and the stability of removal function. However, in the specific field of atmospheric pressure microwave plasma jet machining, this problem needs further systematic research.

In this study first, the optimization of the internal electrode structure was conducted using COMSOL Multiphysics, and the microwave discharge kinetics was simulated. Then ionization and dissociation characteristics of the AMPJ were studied by optical emission spectroscopy (OES). And the optimal carrier gas flow rate was given by combining the data analysis of high-speed camera. The stability of removal function of the designed AMPJ was investigated under the optimal carrier gas flow rate, and the thermal-induced nonlinearity was discussed. Finally, the machining performance of the designed AMPJ was validated on a planar fused silica substrate.

2. Experimental setup

Fig. 1(a) shows the schematic diagram of the inhouse developed atmospheric pressure microwave plasma jet system used in this study, which includes a coaxial microwave torch made of brass. The microwave source frequency for powering the torch is 2.45 GHz with a maximum power of 500 W. The microwave torch internally contains an inner electrode with an outer diameter of 8 mm and an inner diameter of 5 mm. A quartz tube with an inner diameter of 2.0 mm is inserted into

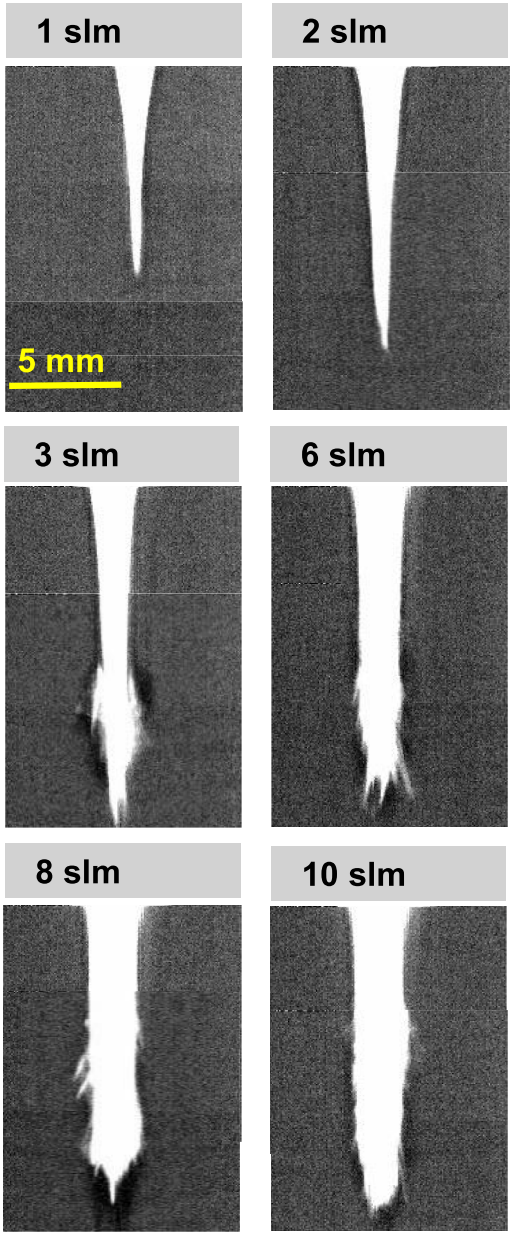

Fig. 5. Plasma jet morphology variation with flow rates of carrier gas.

the inner electrode as the plasma jet channel. During the experiment, the excitation gas Ar (Fujikin Japan Argon 30 slm) and additive gases CF_4, O_2 (Warwick MC-1600L-P-V-4 W CF_4, O_2 100 sccm) were mixed firstly, and then flow into the quartz tube. When the gas flowed through the inner electrode tip, it was ionized by the strong electric field to produce a plasma jet as shown in Fig. 1(b). When the fused silica substrate was processed by the microwave plasma jet, a morning glory jet morphology could be observed as shown in Fig. 1(c), and an axis-symmetric removal spot was formed on the surface of the sample. In this study, the microwave torch was installed on the Z-axis of a three-axis CNC machine tool with an repeated positioning accuracy of 10 μm and a maximum acceleration of 1 G.

In order to characterize the radical distribution characteristics of the plasma jet, the OES spectra were acquired at a position of 10 mm from the outlet of the plasma torch. The collimated emission spectra of the plasma jet were captured using a multimode quartz fiber (FIB-XSR600-Y7J-2.0 Shanghai China) after passing through a collimator. The collected spectra were then analyzed using a spectrometer (OCEAN USB2000+ USA), with an entrance slit width of 10 μm. The spectral data was acquired using Ocean View software, with an integration time of 1 ms. Data averaging is performed every 100 sets. Prior to conducting the experiment, the wavelength response of the spectrometer is calibrated using a mercury-argon lamp, and any noise from the laboratory environment and light sources is removed to ensure accurate spectral acquisition.

The jet morphology is a parameter that affects the machining characteristics. In this study, a high-speed CCD camera (Pco. dimax HD Germany) was used to collect the plasma jet morphology. The microwave plasma jet generated removal function profile and sample surface shape were measured by laser interferometer (Tyggo INF150V-LP Chengdu China), and the thermal accumulation problem during plasma etching was monitored by infrared camera (FILR A655sc USA).

3. Design and evaluation of the microwave plasma torch

The structure of the microwave plasma torch is a key index affecting the discharge symmetry, the bandwidth and the efficiency of energy input. The coaxial portable microwave torch consists of an cylindrical cavity and an inner electrode. The microwave forms a stable standing wave field in the resonant cavity, with the region of enhanced field strength located at the end of the resonant cavity. The tip of the inner electrode is also situated in this region, achieving a secondary concentration of the electric field. This brings the electric field intensity inside the discharge tube to the gas breakdown threshold required, ultimately leading to the formation of a plasma jet. As shown in Fig. 1(a), the discharge gas flows through the inner electrode tip, so the discharge initiation position should be located on the inner surface of the inner electrode. It is ideal that the maximum electric field strength at the tip of the inner electrode is located on the inner surface of the inner electrode. Therefore, the design of an end structure that concentrates the electric field on the inner surface of the inner electrode directly determines the performance of the microwave torch and is the core of whether a high-efficiency plasma jet can be generated.

Therefore, in this section, the electric field distribution at the tip of the inner electrode is obtained through COMSOL Multiphysics simulation. Based on the strength of the electric field at the tip, the optimal structure of the inner electrode is designed. As shown in Fig. 2(a), the type A structure in the figure is the most basic configuration of the inner electrode and one of the four configurations designed in this study. The other three electrode structure are: type B with a straight chamfer at the electric extreme, type C with a circular chamfer applied to the electric extreme, and type D with an atypical geometric structure obtained through spline interpolation. In order to ensure that the model size meets the actual processing requirements. The resonator cavity has a radius of 10 mm, the quartz tube has an inner diameter of 2 mm, and the inner electrode is positioned immediately adjacent to the quartz tube, same as the actual electrode. In this study, the electromagnetic wave module in COMSOL is used for electric field simulation. In order to obtain the relative distribution of the electric field strength within the microwave torch resonant cavity and observe the intensity distribution of the electric field inside the resonant cavity, whether it reaches its maximum at the tip of the inner electrode, the size of the input power only affects the absolute value and has little influence on the relative strength of the electric field. Therefore, the input power used in the electric field simulation is 1 W.

The axial and radial electric field distributions of the four electrodes obtained from the simulation are shown in Fig. 2(b) and (c). As can be seen from the figures, the maximum value of the electric field strength is located at the tip of the inner electrode, and the electromagnetic energy is proportional to the square of the electric field strength. Therefore, the position with the highest electromagnetic wave energy is the most effective position for plasma to obtain energy, and the higher the field strength at this position, the more beneficial it is to improve the ionization efficiency of the microwave torch. The simulation results show

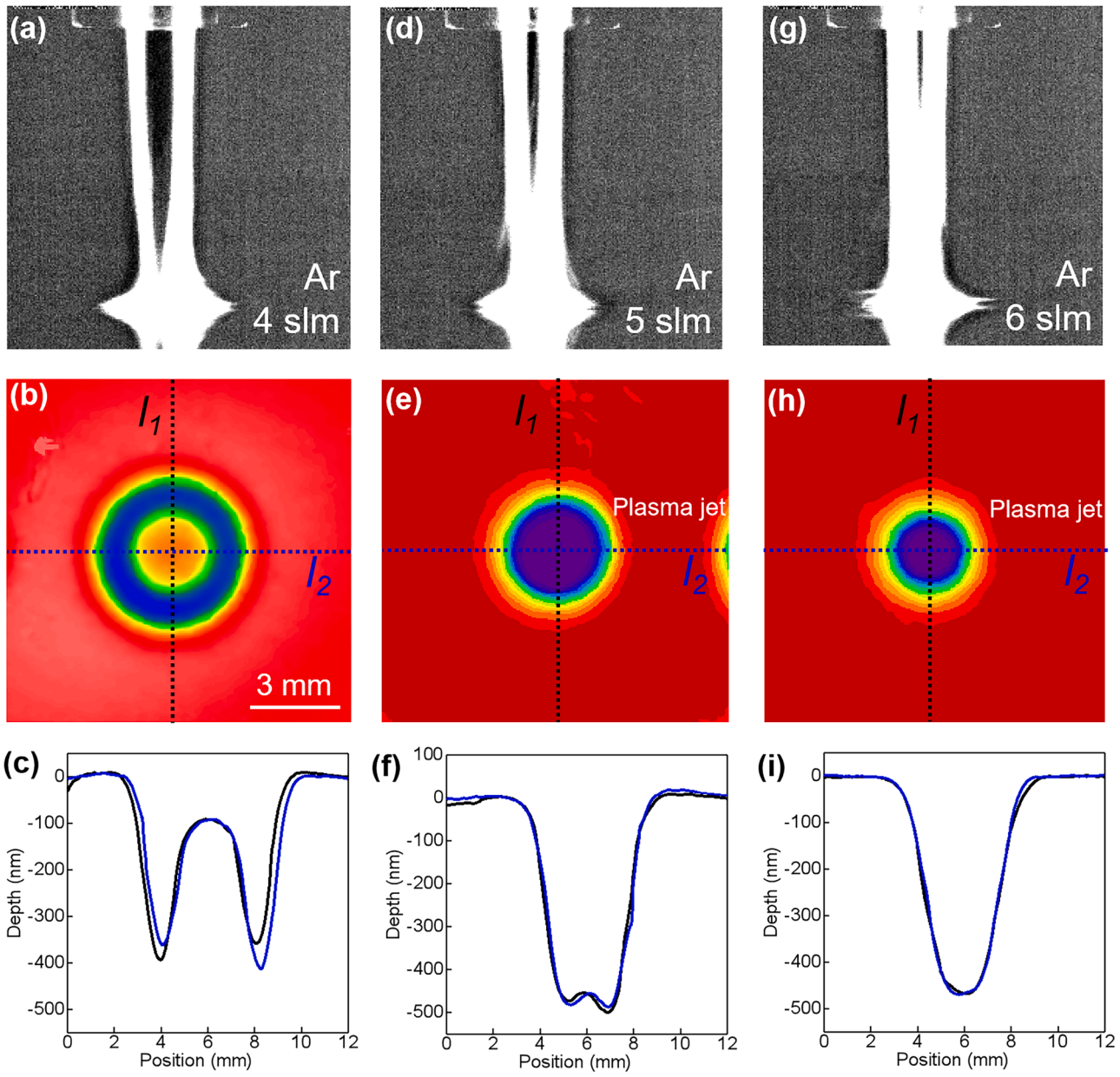

Fig. 6. The plasma jet morphology, material removal morphology and removal function profile. (a,b,c)Ar:CF_4:O_2 = 4000:10:3 sccm case; (d,e,f) Ar:CF_4:O_2 = 5000:10:3 sccm case, and (g,h,i) Ar:CF_4:O_2 = 6000:10:3 sccm case.

that the radial distribution of the electric field of the initial inner electrode structure (type A) has a characteristic where the outer side (Point B) is much higher than the inner side (Point A). This indicates that this inner electrode tip structure is not conducive to the most effective concentration of energy, while the axial distribution shows a trend of first decreasing and then increasing from the inner electrode tip (Point A) to the nozzle outlet (Point C), and has a high field strength, indicating that the plasma is continuously heated in this region. Therefore, a higher field strength in this region is also beneficial to improving the efficiency of the microwave torch. The electric field distribution of type B is similar to that of type A, but the field strength at Point A is higher than that at Point B, and the axial electric field distribution is also the same as that of Type A. The radial electric field distributions of type C and type D indicate that both structures can achieve a reorganization of the radial electric field distribution, with only Point A having the maximum field strength, and type D having the highest field strength at Point A. The axial electric field distribution also shows that type D has the largest electric field strength distribution between Point A and Point C. Compared to type A, the field strength generated at Point A of type D increased by 53.5 %, and the electric field after Point C tends to zero, indicating that this torch has good electromagnetic shielding properties (Table 1).

The excitation process of the plasma significantly impacts macroscopic parameters such as jet morphology and plasma stability. Therefore, simulation on the kinetic processes of plasma excitation was conducted. The simulation was performed using COMSOL Multiphysics. In this study, argon gas was chosen as the working medium. Because of the parameters of the gas discharge reaction are experimental results, it is essential to consider the impact of absolute values. If the power setting is too low, the plasma cannot sustain itself, and the simulation will not converge. At the same time, in order to ensure that the dynamics process obtained by the simulation is similar or even identical to the actual discharge dynamics process, the discharge power is set to 120 W here. Due to the limitation of plasma simulation capability of COMSOL, the simulated size was reduced to 1 mm under atmospheric pressure conditions. However, the desired plasma distribution size to be investigated

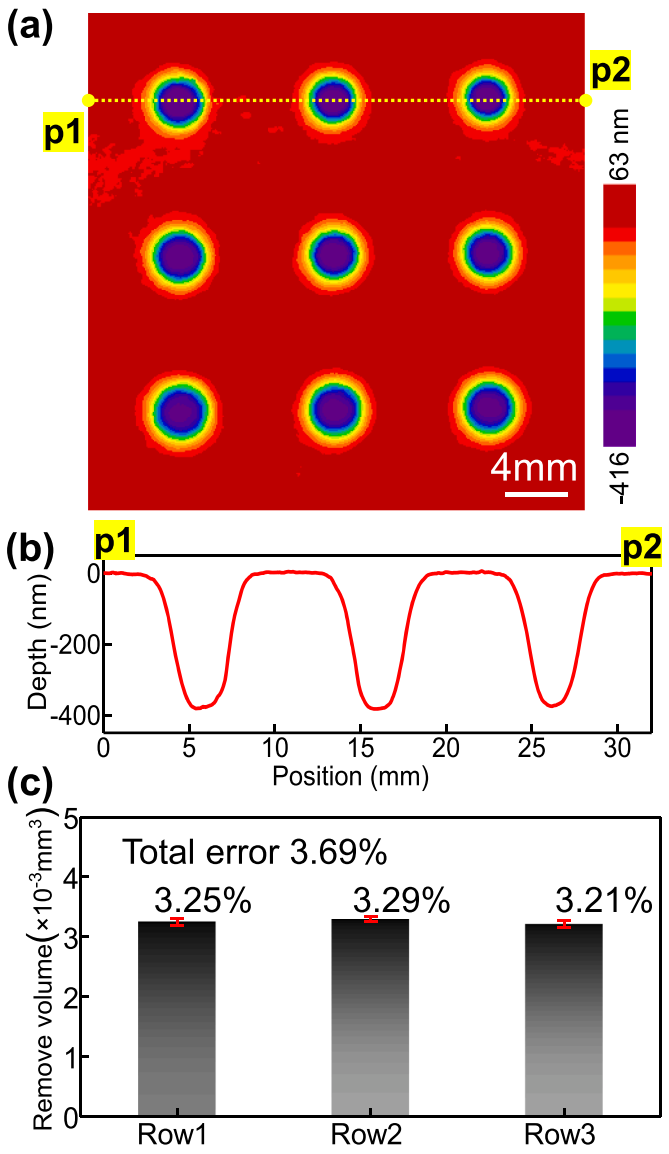

Fig. 7. (a) Single point material removal characteristics, (b) Profile of the removal function, (c) Statistical results of the removal function stability.

in this study is about 5 mm. To ensure the accuracy of the simulation result and the precise of the discharge development kinetics, the discharge pressure is set to 0.2 atm.

In order to reflect the dynamics of the plasma process while considering computational costs, this study simplifies the primary reactions based on the principle of chemical equilibrium. Firstly, the direct ionization reaction of electron collision with the ground state is considered. Secondly, the metastable state of Ar, known for its long lifetime and high density, is involved in multi-step ionization and Penning ionization processes, which significantly affect the discharge process. Therefore, the main reactions involving metastable state participation are included in addition to direct ionization. On the other hand, particle loss is primarily attributed to two reaction processes: collision quenching and wall loss. The wall loss assumes that particles are completely lost upon reaching the wall. The chemical reactions involved in this study are summarized in Table 2.

As shown in Fig. 3(a), the model used for simulation mainly includes a resonant cavity, an inner electrode, and a plasma region (light blue part). As shown in Fig. 3(b), the model is divided into a free quadrilateral mesh, and the mesh of the plasma region is refinement, and the discharge region mesh is further refinement. In this study, the microwave frequency used is 2.45 GHz, which corresponds to a action cycle of 0.408 ns. In order to ensure that the discharge enters a stable stage and take full account of the calculation time, the calculation time in this study is set to 7×10^4 ns, i.e., the calculation period is greater than 10^5.

The simulation results are shown in Fig. 3(c), from the beginning of the calculation to 205 ns, the plasma density in the calculation region remained at the initial density state. When the calculation time increased to 502 ns, the plasma density at the inner electrode tip (Point A) and the bottom plate position (Point C) increased, indicating that gas breakdown occurred and plasma was generated. When the calculation time reached 1005 ns, the excited plasma further developed, and the plasma density between Point A and Point C further increased. When the discharge time increased to 2108 ns, a continuous discharge region was formed between Point A and Point C. After 1×10^4 s, an approximately uniform discharge region was formed between Point A and Point C. From 1×10^4 ns to 7×10^4 ns, the plasma density gradually increased, and the plasma region gradually expanded to the vicinity of the discharge tube axis. Within the time range of 5×10^4 ns to 7×10^4 ns, the shape of the plasma region changed little, but the density increased, indicating that the discharge had shifted from a rapid development stage to a dynamic equilibrium stage, and then a stable plasma was formed.

The results show that the discharge occurs simultaneously from point A and point C, first develops towards each other to form a linear discharge region, and then expands towards the position of the discharge tube axis, eventually filling the entire discharge tube. Therefore, the electric fields at point A and point C jointly determine the dynamic process of plasma excitation and development. When optimizing the design of the microwave torch, it is necessary to consider the field distribution at both point A and point C.

In the field of ultra-precision machining, the priority of machining accuracy is higher than that of machining efficiency. This paper is committed to pursuing high machining accuracy; therefore, it adopts a process combination scheme of adding a small flow of reactive gas (CF_4) to a large carrier gas (Ar) flow, optimizing the machining efficiency appropriately while prioritizing the assurance of machining accuracy.

In order to verify the ionization and dissociation characteristics of CF_4 by the newly developed microwave torch, OES was used to investigate the influence of additive gas content on the radical composition of the plasma jet. In this section, carrier gas flow rate set to 9 slm, discharge power set to 120 W.

As is shown in Fig. 4, in pure Ar discharge, the plasma spectrum mainly distributes in the range of 600 to 900 nm, which is a typical Ar plasma spectrum. In addition, a small number of spectral peaks in the range of 300–350 nm are due to the excitation radiation spectrum produced by the entrainment of water vapor and nitrogen in the atmosphere. When CF_4 is added to the Ar plasma, obvious radiation peaks appear in the 350 nm and 550 nm bands of the plasma spectrum. The 350–450 nm band is the characteristic spectrum section of CF_x, while the 516.7 nm peak is the characteristic peak of C_2. This phenomenon indicates that microwave torch can cause dissociation and ionization of CF_4. The essence of plasma processing is chemical reaction including deposition and etching. The radical component governing the deposition process is CF_x, and deposition can lead to micro-masking problem affecting the roughness of the sample surface after etching. Therefore, it is necessary to inhibit the formation of CF_x components. To this end, the effect of adding O_2 components to the microwave Ar:CF_4 reaction system on CF_x components was further studied. As can be seen from Fig. 4, a small amount of O_2 addition can significantly reduce the content of CF_x and C_2, and with the increase of O_2 content, the intensity of CF_x and C_2 components in the plasma will further decrease, indicating that O_2 can effectively inhibit the formation of CF_x components. Therefore, the subsequent plasma etching process all adopts the mixture gas of Ar, CF_4 and O_2.

The plasma jet morphology greatly affect the plasma machining performance, thus, the plasma jet morphology was captured using a high

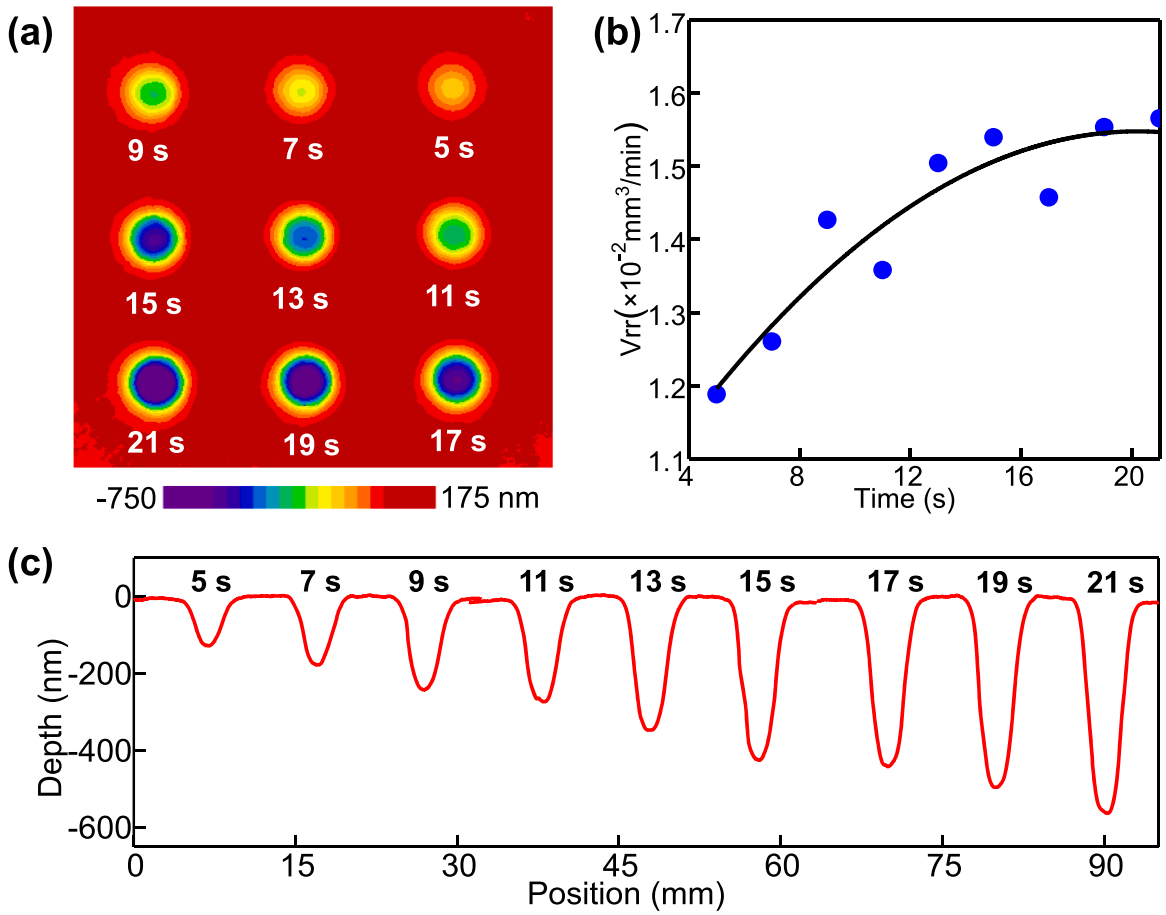

Fig. 8. (a) Removing function arrays under different dwell times, (b) Variation of volume removal rate over time, (c) Removal function profile of dwell points under different dwell times.

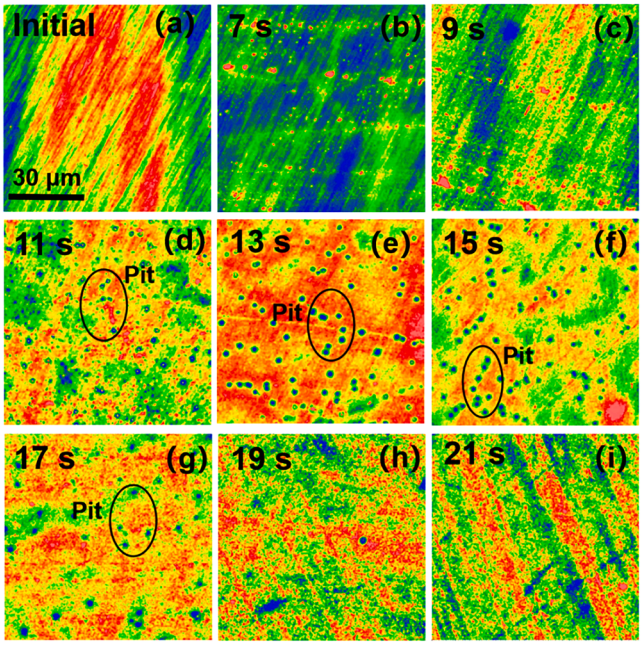

Fig. 9. The morphology of the etched spot centers at various dwell times.

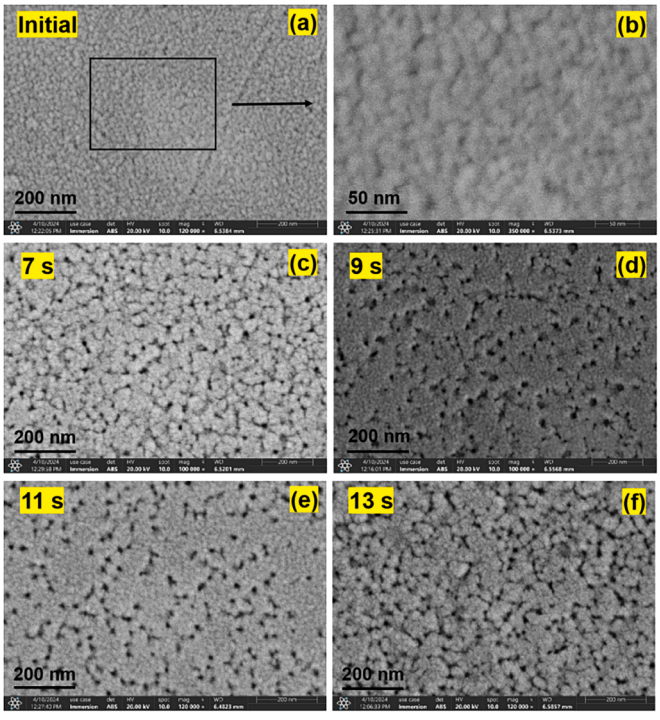

Fig. 10. The changes in surface morphology of samples before and after plasma etching using SEM.

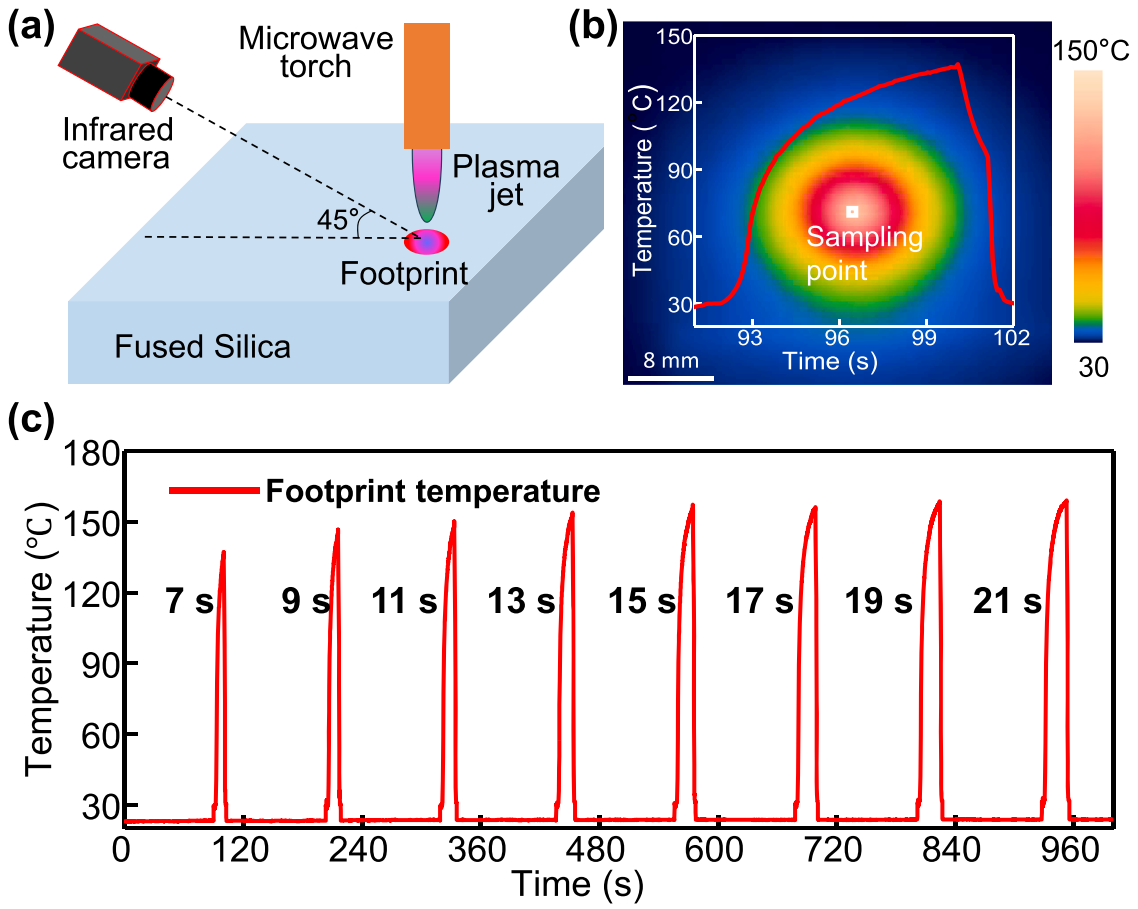

Fig. 11. (a) Schematic diagram of temperature measurement setup, (b) The temperature distribution of the dwell point and the maximum temperature evolution with time, (c) The maximum temperature variation of the dwell points in different dwell time.

speed CCD camera. Considering the issue of plasma brightness, the high-speed camera was set with an integration time of 100 μs and a frame rate of 1000. The camera focal plane was aligned with the jet axis. Based on the data obtained from the high-speed camera, the influence of carrier gas flow rate on the jet morphology was investigated. During the experiment, the discharge power was maintained at a constant value of 120 W, while the gas flow rate was varied from 1 to 10 slm.

Fig. 5 shows the plasma jet morphology under different Ar flow rates. As can be observed from the figure, at flow rates of 1 slm and 2 slm, the plasma jet exhibits typical laminar characteristics, with a conical shape. However, when the flow rate increases to 3 slm, a transition occurs in the plasma jet, and turbulent characteristics appear at the jet tail. Subsequently, as the flow rate continues to increase, the transition point advances. It is evident that the morphology of the turbulent state is highly disordered. In plasma machining, it is desirable for the jet morphology to be stable, or laminar flow condition. However, subsequent experiments have shown that when introducing CF_4 and O_2 components in a laminar state plasma, the plasma becomes unstable due to the quenching effects. Therefore, in practical processing scenarios, the carrier gas flow rate was determined by the uniformity of the machining performance rather than the flow state of the plasma jet.

4. Machining performance of the AMPJ

4.1. Material removal characteristics and surface morphological evolution

The material removal characteristics of atmospheric microwave plasma jets are key indicators affecting the quality of processing. Fig. 4 in this article has shown that reactive particles are produced in the plasma when CF_4 and O_2 are added to the Ar plasma. Since the plasma etching rate is low when Ar is set to 9000 sccm, the CF_4 flow is increased to 10 sccm and the O_2 flow is set to 3 sccm to improve the etching rate, while reducing the Ar flow. Due to the quenching effect of CF_4 and O_2 on Ar plasma, when the argon flow is reduced to 4 slm, the plasma jet shows a serious "hollow" effect (Fig. 6a) and surge phenomenon. The material removal morphology presents a circular shape, and the removal function profile is a significant "W" shape. As the flow rate of Ar gas increases, the relative concentration of reactive gases decreases, and the quenching effect weakens. The "hollow" phenomenon gradually diminishes, as shown in Fig. 6d. When the Ar gas is at 5 slm, the hollow region is significantly smaller than that at 4 slm, and the etching area exhibits a flat-bottomed characteristic (Fig. 6e). Fig. 6f shows that there is a small protrusion at the center of the removal function at this time. When the Ar flow rate is increased to 6 slm, the "hollow" issue with the plasma jet essentially disappears. Figs. 6h and i show that at this point, the removal function assumes a typical Gaussian shape, while the etching depth is similar to that at the 5 slm condition.

Generally, a Gaussian-shaped removal function morphology has stronger processing capabilities. Therefore, the process parameters were optimized to Ar 6 slm, CF_4:10 sccm, and O_2:3 sccm with a constant input power of 120 W. The plasma jet was used to form 9 etching spots on a fused silica substrate with a single point dwell time of 10 s and an interval of 120 s. The results are shown in Fig. 7. The dwell points exhibit axial symmetry characteristics which is desirable in optical figuring. Fig. 7(b) shows the contour of the removal function, which exhibits a Gaussian shape with full width at half maximum (FWHM) of 3.2 mm. Fig. 7(c) provides the statistical results of the removal volume for each column of removal points, revealing fluctuations of about 3.3% for each column. The statistical results for the three columns points indicate a total fluctuation of 3.69%. Compared to the 10% to 30% volume

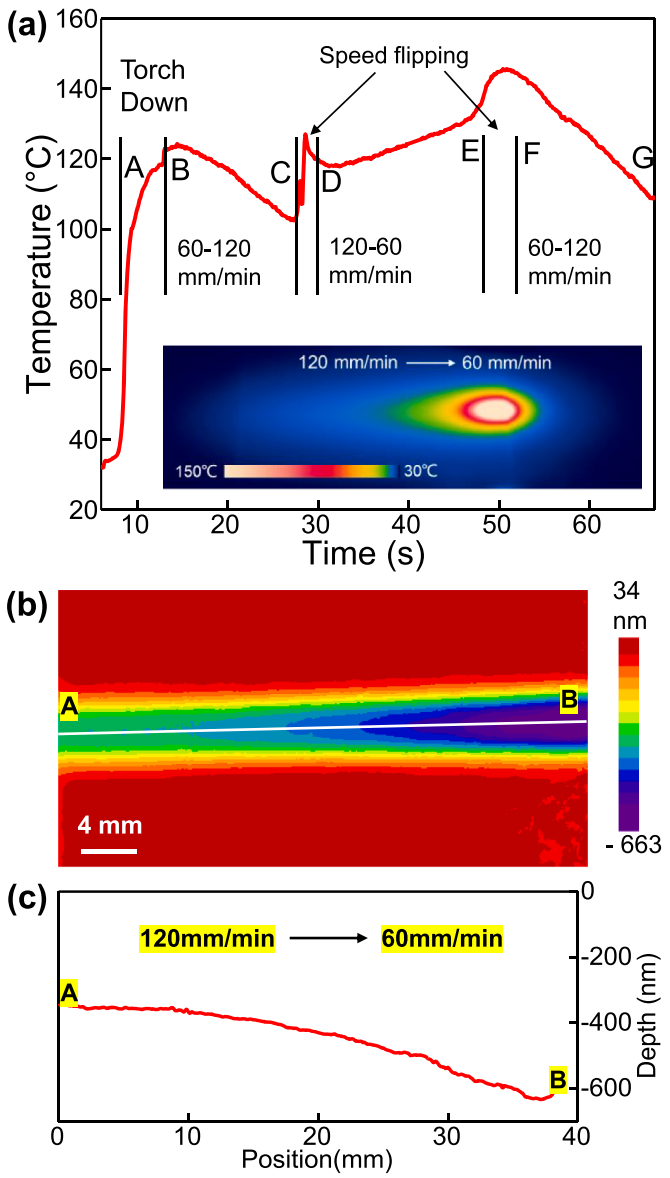

Fig. 12. (a) Temperature variation with scanning speed, (b) Trench formed by variable-rate etching, (c) Etching depth variation with speed.

removal rate fluctuations produced by IOM-developed microwave plasma jets during fused silica processing [36], the microwave torch developed in this paper has the characteristic of producing high stability material removal.

Subsequently, single-point removal experiments with different dwell times was carried out, starting with an initial dwell time of 5 s and a time interval of 2 s. The experimental results are shown in Fig. 8. It is clear that as the dwell time increases, the removal depth significantly increases. However, the curve depicting removal rate over time in Fig. 8 (b) reveals that as the dwell time increases, the removal rate exhibits a nonlinear increasing trend and eventually stabilizes. As is shown in Fig. 8(c), the removal function profile under different dwell times exhibits a Gaussian shape, and the removal depth also demonstrates a nonlinear increasing trend over time.

To study the impact of plasma etching on the surface morphology of samples. We image of each dwell point center in Fig. 8a was taken using a white-light interferometer, the result is shown in Fig. 9. It is clear shown in Fig. 9b to Fig. 9c that when dwell time increase from 7 s to 9 s, the bottom of the dwell points shows a striped morphology similar to the original surface (Fig. 9a). However, when dwell time increases to 11 s, the etch depth reaches 273 nm, and an etching pit appears at the bottom of the dwell point (Fig. 9d). When the etch depth exceeds 496 nm (Fig. 9g), the etching pits at the bottom of the etched spots disappear. It is suggesting that this depth range of 273 nm to 496 nm corresponds to the thickness of the subsurface damage layer caused by the previous process. And surface roughness without etching pits decrease from Sa 1.92 nm in 19 s (Fig. 9h) to Sa 1.58 nm in 21 s (Fig. 9i). Therefore, it is beneficial to obtain high quality surface by appropriately increasing the etching depth.

In order to further observe the surface morphology of the sample after plasma etching, scanning electron microscopy (SEM) was used to capture images of the sample surface. The results are shown in Fig. 10. From Figs. 10a and 10b, it is evident that the original surface has a smooth undulating structure. However, as shown in Figs. 10c to 10f, the areas etched by plasma clearly display the appearance of tiny etch pits with a scale of about 20 nm and microcracks on the sample surface. The size of the etch pits does not change with etching time, but the density of the etch pits shows some variation with increasing etching time. Therefore, addressing the issue of the small etch pits on the sample surface after plasma etching is a core problem in further improving the quality of plasma processing in subsequent research.

4.2. Nonlinear material removal mechanisms and planarization processing characteristics

To investigate the cause of nonlinear removal, infrared camera was used to collect the temperature distribution characteristics at the dwell point, as shown in Fig. 11. Fig. 11(a) shows a schematic diagram of the experimental system, in which the angle between the optical axis of the infrared camera and the sample plane was 45°, and the emissivity of the sample was set to 0.95.

The collected temperature distribution at the dwell point is shown in Fig. 11(b), which exhibits a typical axial symmetry characteristic. The red curve in the figure represents the temperature change curve with time, and the temperature sampling point was at the centre of the dwell point. The curve shows that at the initial heating moment, the surface temperature of the sample rapidly increases, and then the rate of increase gradually decreases. After the torch is lifted (at the position of 100 s), the temperature dropped rapidly. As shown in Fig. 11(c), it shows that with increasing dwell time, the maximum temperature at the centre of the dwell point gradually increases but the rate of increase decreases.

Plasma etching is a purely chemical process, and the etching rate will increase rapidly with temperature. Therefore, as the dwell time increases, the maximum temperature at the dwell point gradually increases, and the corresponding etching rate also increases. As a result, the volumetric removal rate increases. After 15 s, the maximum temperature at the dwell point is almost the same, so the volume removal rates are similar. These results coincide with the measured variation of Vrr with time shown in Fig. 8(b).

In actual machining process, the plasma jet usually scans on the substrate with different speeds rather than point-to-point dwelling. Therefore, the thermal effect during plasma jet scanning was studied. The microwave torch was fixed, and the substrate accelerated and decelerated along the X-axis (speed range: 60 to 120 mm/min). The temperature variation is shown in Fig. 12(a). The A-B section represents the plasma jet down stroke phase, during which the surface temperature of the sample rapidly increases from room temperature to 120 °C. As can be seen from the B-C section, as the speed increases, the dwell point temperature decreases accordingly, and exhibits a clear nonlinear effect. At point C, when the sample speed reaches 120 mm/min, it then undergoes the C-D section, where the sample speed reverses and reaches 120 mm/min at point D. After that, it undergoes the D-E section and decelerates to 60 mm/min. The higher temperature at point D is due to the dwell of the microwave torch during the speed reversal process, resulting in heat accumulation and temperature increase. Afterwards, as the speed decreases, the surface temperature of the substrate

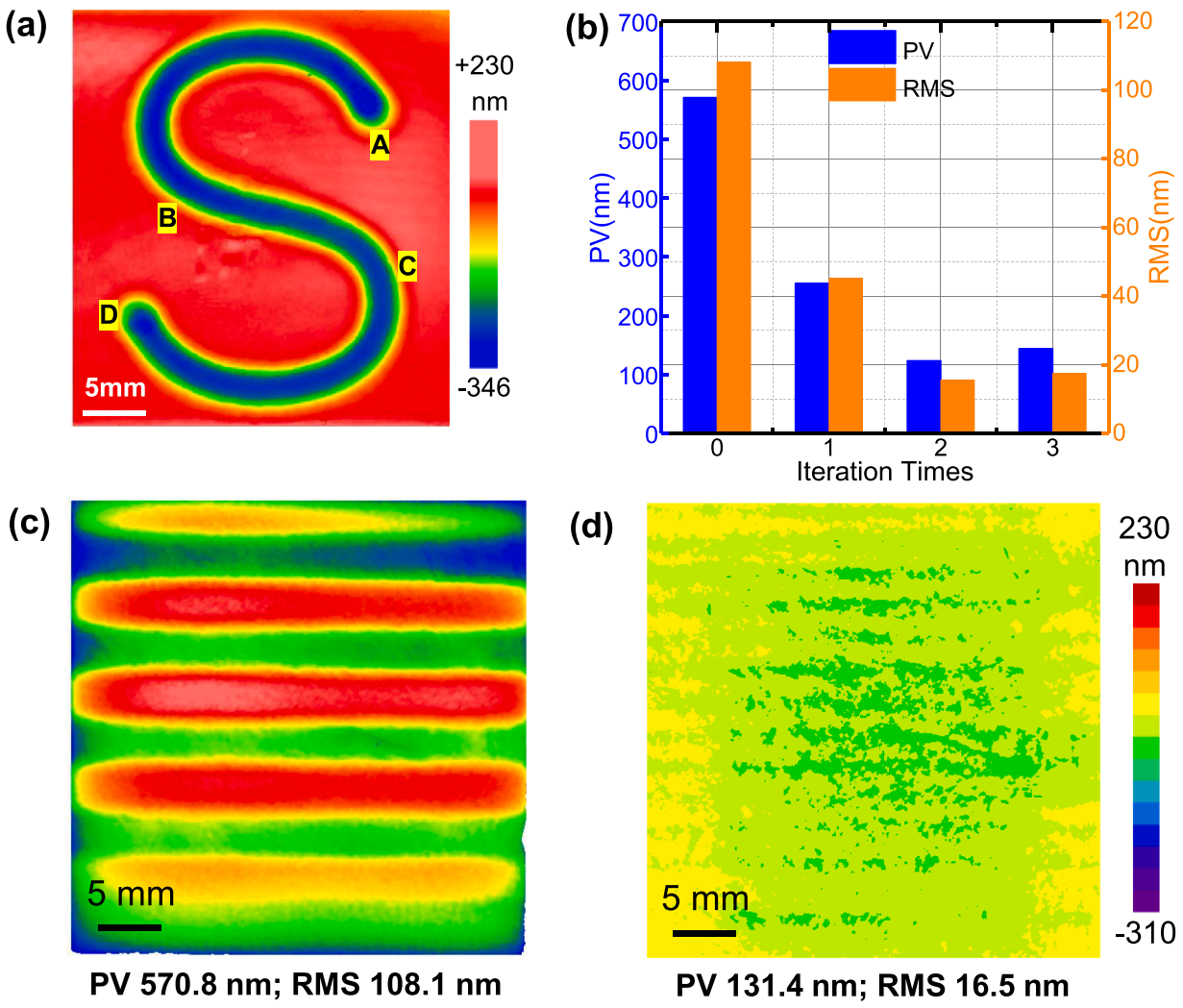

Fig. 13. (a) Letter "S" written by the microwave torch measured by laser interferometer, (b) PV and RMS after different AMPJ machining iterations, (c, d) The surface error distribution before and after AMPJ machining.

approximately linearly increases. The E-F stage is similar to the C-D stage, but due to the lower velocity, the cumulative heating effect is more significant, causing the temperature at point F to be significantly higher than that at point D. Subsequently, the sample accelerates from 60 mm/min to 120 mm/min, i.e., the F-G section, during which the dwell point temperature approximately linearly decreases.

The above results show that the temperature at the dwell point approximately linearly decreases with speed and exhibits a significant cumulative heating effect during speed reversal. Since plasma etching is a purely chemical reaction process, the etching rate is governed by the Arrhenius equation, and the etching rate under different motion rates will exhibit significant nonlinear effect. Fig. 12(b) shows the trench formed by variable-rate etching, and Fig. 12(c) shows the etching profile along the A-B direction in Fig. 12(b). It can be seen that the etching depth non-linearly increases with decreasing motion speed.

To verify the processing performance of the microwave torch, fundamental machining operations like letter writing and surface figuring were carried out. Fig. 13(a) shows the letter "S" written using the microwave torch with a scanning speed of 100 mm/min. It means that the design plasma jet is capable to process continuously variable curvature structures. However, the differences in dwell time caused by different radii of curvature in AB, BC, and CD sections result in different depths of removal, this result is also due to the thermal effect which needs to further studied in the future. Furthermore, combined with the nonlinear dwell time inversion algorithm, a fused silica planar figuring experiment was conducted using the plasma jet, and the results are shown in Fig. 13(b~d). After two iterations of AMPJ figuring, the surface form error decreased from PV 570.8 nm and RMS 108.1 nm, to PV 131.4 nm and RMS 16.5 nm. Those results demonstrates that the design microwave torch has good machining capabilities towards fused silica substrates.

5. Conclusions

This paper introduces a novel microwave torch internal electrode structure and the discharge dynamics of the torch is investigated. Subsequently, the effect of Ar carrier gas flow rate on jet morphology is studied using high-speed cameras, and the influence of adding gases (CF_4, O_2) on plasma composition is presented. Finally, the characteristics of the torch in optical machining are explored. The main research results are as follows:

1) Simulation results revealed that a spline curve electrode enables electric field reorganization, resulting in a 54 % increase in electric field intensity. Plasma discharge simulation results showed that the plasma was excited at both the inner electrode tip and the bottom of the resonant cavity, and then expanded between the two excitation positions to form a "linear" discharge region. Finally, it gradually extended along the axis of the discharge tube to form a stable plasma discharge zone.

2) Experiments using newly designed microwave torch discharge experiments show that when Ar gas is set in 1 slm and 2 slm, the jet exhibited laminar flow, while at flow rates greater than 2 slm, turbulent flow was observed at the jet tail. The transition point increased with increasing flow rate, and turbulence tended to be uniform in all directions. When CF_4 was added to the Ar plasma, CF_x and C_2 characteristic spectral bands appeared in the spectrum, indicating that CF_4 was effectively dissociated. Furthermore, due to the quenching effect of CF_4 on Ar excited states, the intensity of the Ar spectrum decreased. When O_2 was further added to the plasma, due to oxidation, the contents of CF_x and C_2 significantly decreased, and the larger the O_2 content, the lower the CF_x and C_2 contents.
3) Experiments on microwave plasma jet machining show that the removal function profile presents Gaussian shape and material removal stability reached 3.69 %. Due to the nonlinear increase in dwell point temperature with dwell time, the removal rate initially increased and then tended to stabilize. Different heat accumulation occurred under variable speed conditions, resulting in a nonlinear increase in etching depth with decreasing velocity. The "S" written using the microwave torch indicates that the processing system has the ability to process continuously variable curvature structures. Further, machining experiments conducted using this system show that this torch can make the initial grooves surface with PV 570.8 nm, RMS 108.1 nm, to plane surface with PV 131.4 nm, RMS 16.5 nm.

CRediT authorship contribution statement

Chuansheng Wang: Writing – review & editing, Writing – original draft, Visualization, Validation, Supervision, Software, Methodology, Investigation, Formal analysis, Data curation, Conceptualization. **Bing Wu:** Visualization. **Wei Hang:** Resources, Funding acquisition. **Dong Lu:** Visualization. **Hui Deng:** Writing – review & editing, Writing – original draft, Visualization, Validation, Resources, Funding acquisition, Data curation, Conceptualization.

Declaration of competing interest

The authors declare that they have no known competing financial interests or personal relationships that could have appeared to influence the work reported in this paper.

Data availability

No data was used for the research described in the article.

Acknowledgments

This work is supported by the National Key Research and Development Program of China (2023YFE0202900), the National Natural Science Foundation of China (52035009), the research fund from the Science, Technology and Innovation Commission of Shenzhen Municipality (JCYJ20200109141003910, JCYJ20210324120402007), Shenzhen, China. The author acknowledges the assistance of SUSTech Core Research Facilities. The present study was also supported by Shenzhen Engineering Research Center for Semiconductor-specific Equipment.

References

[1] R.E. Parks, L.D. Bollinger, G. Steinberg, C.B. Zarowin, Rapid optical figuring of aspherical surfaces with plasma-assisted chemical etching, Large Optics II 1618 (1992) 14–21.
[2] G.M. Sanger, et al., Rapid noncontact optical figuring of aspheric surfaces with plasma-assisted chemical etching, Adv. Opt. Manuf. Test. 1333 (1990) 43–57.
[3] C. Gorecki, et al., Plasma surface figuring of large optical components, in: Presented at the Optical Micro- and Nanometrology IV, 2012 843011.
[4] T. Arnold, G. Boehm, I.-M. Eichentopf, M. Janietz, J. Meister, A. Schindler, Plasma jet machining, Vakuum Forschung Praxis 22 (2010) 10–16.
[5] R.C. Machado, A.B.S. Silva, G.L. Donati, A.R.A. Nogueira, Multi-energy calibration as a strategy for elemental analysis of fertilizers by microwave-induced plasma optical emission spectrometry, J. Anal. Atom. Spectrom. 33 (2018) 1168–1172.
[6] J. Nelson, G. Gilleland, L. Poirier, D. Leong, P. Hajdu, F. Lopez-Linares, Elemental analysis of crude oils using microwave plasma atomic emission spectroscopy, Energy Fuel. 29 (2015) 5587–5594.
[7] A.Y. Hui, G. Wang, B. Lin, W.T. Chan, Microwave plasma treatment of polymer surface for irreversible sealing of microfluidic devices, Lab. Chip. 5 (2005) 1173–1177.
[8] S. Sato, et al., Surface-nitriding treatment of steels using microwave-induced nitrogen plasma at atmospheric pressure, Appl. Surf. Sci. 258 (2012) 7574–7580.
[9] C. Chaichumporn, P. Ngamsirijit, N. Boonklin, K. Eaiprasetsak, M. Fuangfoong, Design and construction of 2.45GHz microwave plasma source at atmospheric pressure, Procedia Eng. 8 (2011) 94–100.
[10] J. Henriques, N. Bundaleska, E. Tatarova, F.M. Dias, C.M. Ferreira, Microwave plasma torches driven by surface wave applied for hydrogen production, Int. J. Hydrog. Energy 36 (2011) 345–354.
[11] Y. Dong, J. Zhang, P. Zhang, H. Tian, D. Yu, Jet morphology analysis of microwave-generated plasma for microfabrication of optics, Plasma Process. Polym. (2022) 1–14.
[12] W.J. Liu CHanglin, Xiong Liwei, Liu Fan, Design and experiment of an atmosphere microwave plasma torch device, Chin. J. Low Temp. Phys. 33 (2011) 112–115.
[13] C.P. Hancock, N. Dharmasiri, M. White, A.M. Goodman, The design and development of an integrated multi-functional microwave antenna structure for biological applications, IEEE T. Microw. Theory 61 (2013) 2230–2241.
[14] S.R. Wylie, A.I. Al-Shamma'a, J. Lucas, R.A. Stuart, An atmospheric microwave plasma jet for ceramic material processing, J. Mater. Process. Technol. (2004) 153–154.
[15] T. Konishi, Y. Oshita, K. Itoh, Ultrafast optical distortion equalizer using time–frequency domain processing, J. Lightw. Technol. 24 (2006) 2693–2700.
[16] K. Yamamura, S. Shimada, Y. Mori, Damage-free improvement of thickness uniformity of quartz crystal wafer by plasma chemical vaporization machining, CIRP Ann.-Manuf. Technol. 57 (2008) 567–570.
[17] Marco Castelli, Renaud Jourdain, Paul Morantz, Paul Shore, Fast figuring of large optics by reactive atom plasma, in: Proc. of SPIE 8450, 2013 845034.
[18] H.H. Achim Stephan, Cutting human tissue with novel atmospheric pressure microwave plasma jet, in: Proceedings of the 46th European Microwave Conference, 2016, pp. 902–905.
[19] A. Lehmann, F. Pietag, T. Arnold, Human health risk evaluation of a microwave-driven atmospheric plasma jet as medical device, Clin. Plasma Med. (2017) 7–8.
[20] T. Arnold, G. Böhm, Application of atmospheric plasma jet machining (PJM) for effective surface figuring of SiC, Precis. Eng. 36 (2012) 546–553.
[21] R. Navarro, J.H. Burge, T. Arnold, G. Böhm, H. Paetzelt, Nonconventional ultra-precision manufacturing of ULE mirror surfaces using atmospheric reactive plasma jets. Advances in Optical and Mechanical Technologies For Telescopes and Instrumentation II, 2016, p. 99123N.
[22] H. Paetzelt, G. Böhm, T. Arnold, Etching of silicon surfaces using atmospheric plasma jets, Plasma Sources Sci. Technol. 24 (2015) 025002.
[23] P. Piechulla, J. Bauer, G. Boehm, H. Paetzelt, T. Arnold, Etch mechanism and temperature regimes of an atmospheric pressure chlorine-based plasma jet process, Plasma Process. Polym. 13 (2016) 1128–1135.
[24] T. Arnold, G. Böhm, H. Paetzelt, Ultra-precision surface machining with reactive plasma jets, Contrib. Plasm. Phys. 54 (2014) 145–154.
[25] B. Georg Boehma, H. Muellera, and T. Arnold, Manufacturing of freeform optics completely based on plasma jet machining, 2021 JTu3B.
[26] J. Meister, T. Arnold, New process simulation procedure for high-rate plasma jet machining, Plasma Chem. Plasma. P. 31 (2010) 91–107.
[27] J. Meister, G. Böhm, I.-M. Eichentopf, T. Arnold, Simulation of the substrate temperature field for plasma assisted chemical etching, Plasma Process. Polym. 6 (2009) S209–S213.
[28] J.M. Th Arnold, G. Böhm, Atmospheric plasma jet machining: simulation of SpatioTemporal substrate surface temperature distributions, in: 2008 OSA /FiO/LS/META/OF&T, 2008.
[29] A. Efremov, J. Lee, J. Kim, On the control of plasma parameters and active species kinetics in $CF_4 + O_2 +$ Ar Gas Mixture by CF_4/O_2 and O_2/Ar mixing ratios, Plasma Chem. Plasma Process. 37 (2017) 1445–1462.
[30] Ž. Nikitović, V. Stojanović, Z.L. Petrović, U. Cvelbar, M. Mozetič, Transport coefficients for electron scattering in CF_4/Ar/O_2 mixtures with a significant presence of F_x or CF_x radicals, EPL 91 (2010) 55001.
[31] A. Dias, et al., Production of N-graphene by microwave N_2-Ar plasma, J. Phys. D 49 (2016) 055307.
[32] Y. Wang, et al., Design of a fully automatic microwave plasma torch system, Rev. Sci. Instrum. 90 (2019) 055112.
[33] V. Léveillé, S. Coulombe, Design and preliminary characterization of a miniature pulsed RF APGD torch with downstream injection of the source of reactive species, Plasma Sources Sci. Technol. 14 (2005) 467–476.
[34] H.S. Park, S.J. Kim, H.M. Joh, T.H. Chung, S.H. Bae, S.H. Leem, Optical and electrical characterization of an atmospheric pressure microplasma jet with a capillary electrode, Phys. Plasmas 17 (2010) 033502.
[35] G. Arnoult, R.P. Cardoso, T. Belmonte, G. Henrion, Flow transition in a small scale microwave plasma jet at atmospheric pressure, Appl. Phys. Lett. 93 (2008) 191507.
[36] Faezeh Kazemi, Georg Boehm, Thomas Arnold, Ultra-precise surface machining of N-BK7® using microwave-driven reactive, in: Proc. of SPIE 11385, 2019 1138509.